

THE FAR INFRARED EMISSION OF THE FIRST MASSIVE GALAXIES

MARIA EMILIA DE ROSSI^{1,2}, GEORGE H. RIEKE³, IRENE SHIVAEI³, VOLKER BROMM⁴,
AND JIANWEI LYU³

Draft v5.0

ABSTRACT

Massive Population II galaxies undergoing the first phase of vigorous star formation after the initial Population III stage should have high energy densities and silicate-rich interstellar dust. We have modeled the resulting far-infrared spectral energy distributions (SEDs), demonstrating that they are shifted substantially to bluer (“warmer”) wavelengths relative to the best fitting ones at $z \approx 3$, and with strong outputs in the 10 – 40 μm range. When combined with a low level of emission by carbon dust, their SEDs match that of Haro 11, a local moderately-low-metallicity galaxy undergoing a very young and vigorous starburst that is likely to approximate the relevant conditions in young Population II galaxies. We expect to see similar SEDs at high redshifts ($z \gtrsim 5$) given the youth of galaxies at this epoch. In fact, we find a progression with redshift in observed galaxy SEDs, from those resembling local ones at $2 \lesssim z < 4$ to a closer resemblance with Haro 11 at $5 \lesssim z < 7$. In addition to the insight on conditions in high redshift galaxies, this result implies that estimates of the total infrared luminosities at $z \sim 6$ based on measurements near $\lambda \sim 1$ mm can vary by factors of 2 – 4, depending on the SED template used. Currently popular modified blackbodies or local templates can result in significant underestimates compared with the preferred template based on the SED of Haro 11.

Subject headings: galaxies: high-redshift – evolution – abundances – infrared: galaxies

1. INTRODUCTION

The far-infrared (FIR) spectral energy distributions (SEDs) of star-forming galaxies provide unique clues to the state of their interstellar medium (ISM), as well as to the process of star formation within them. For example, Sauvage & Thuan (1992) and Popescu et al. (2011) model the radiative transfer in star forming galaxies, showing how the basic behavior can be explained in terms of two underlying components: 1) warm and localized dust heated by very young stars and with an SED peaking in the 50 – 100 μm range, and 2) cooler and diffuse dust heated by an older stellar population with an SED peaking in the 100 – 200 μm range. SED templates show that the relative role of the first component increases as the luminosity in young stars increases, with the warm component dominating in luminous and ultraluminous infrared galaxies (LIRGs and ULIRGs) (Rieke et al. 2009). For the highest luminosity *local* galaxies, the mid-infrared ($\lambda < 30$ μm) emission is suppressed (e.g., Rieke et al. 2009) by optical depth effects arising from the extreme ISM densities in the star-forming regions (e.g., da Cunha et al. 2010). At *moderate redshifts* ($1 \lesssim z < 3$), there is less of this suppression and the SEDs even of ULIRGs resemble those of local LIRGs (Symeonidis et al. 2009, 2013; Rujopakarn et al. 2013; Kirkpatrick et al. 2015). At $z \sim 2$, the suppression due to high optical depth begins only at luminosities $\gtrsim 3 \times 10^{12} L_{\odot}$, an order of magnitude more luminous than locally (Shipley et al. 2016). This

behavior seems to be connected with the greater extent of the FIR sources in the very luminous infrared galaxies at these redshifts, compared with those in local galaxies of similar luminosity (Rujopakarn et al. 2011; Shipley et al. 2016). In addition, Schreiber et al. (2018) demonstrate a reduction in the peak wavelength (i.e., an increase in the equivalent temperature) of the far-infrared SEDs of star forming galaxies with redshift from $z \lesssim 1$ to $z \simeq 3.5$.

However, the behavior of star forming galaxy far-infrared SEDs at $z \gtrsim 3$ is not well characterized and thus cannot yet be used for similar insights about them. In general, relatively little information is available to model the SEDs, so the behavior has been described in simplified ways. Wang et al. (2007) fitted the FIR SEDs (assumed to be powered by star formation) for high redshift quasars with a modified blackbody of temperature 47 K and emissivity index $\beta = 1.6$. These parameters have been adopted by many subsequent works (e.g., Leipski et al. 2014; Willott et al. 2017). Bowler et al. (2018) used a similar approach but with a fiducial temperature of 40 K. Lyu et al. (2016) found that template fits to the SEDs of high redshift quasars were improved dramatically by using the relatively warm SED of the low metallicity, extreme star-forming galaxy Haro 11, in place of modified blackbodies or the colder templates that apply at redshifts up to 2 – 3. Faisst et al. (2017) used indirect arguments to conclude that the FIR SEDs of very high redshift galaxies in general are “hotter” than those of local galaxies. Yuan et al. (2015) used color-color diagrams in the SPIRE bands (250, 350, and 500 μ) to show that by $z = 5 - 6$ none of the templates they considered (Chary & Elbaz 2001; Dale & Helou 2002; Elbaz et al. 2011; Magdis et al. 2012; Berta et al. 2013; Ciesla et al. 2014) were consistent with the data.

A trend toward warmer SEDs would arise from the increasing temperature of the cosmic microwave back-

¹ Universidad de Buenos Aires, Facultad de Ciencias Exactas y Naturales y Ciclo Básico Común. Buenos Aires, Argentina

² CONICET-Universidad de Buenos Aires, Instituto de Astronomía y Física del Espacio (IAFE). Buenos Aires, Argentina

³ Steward Observatory, Department of Astronomy, University of Arizona, 933 North Cherry Avenue, Tucson, AZ 85721

⁴ Department of Astronomy, The University of Texas, 2515 Speedway, Stop C1400, Austin, Texas 78712-1205

ground (CMB) with increasing redshift (da Cunha et al. 2013). However, given the high temperatures we find for the SEDs (> 40 K at $z \approx 6$), the effect is not large enough to explain the observed behavior; see fig. 5 of da Cunha et al. (2013). As an example, we have applied equation (12) of da Cunha et al. (2013) to parameters for the coldest dust contributing to the peak of the SED ($T = 44$ K, $\beta = 1.2$) that would maximize the CMB contribution for Haro 11 (suggested as a suitable high redshift template by Lyu et al. (2016)). We find that the CMB would raise the dust temperature at $z = 6$ by $< 1\%$. Any perceptible effect of the CMB would be modest and confined to the mm-wave regime (da Cunha et al. 2013). Strandet et al. (2016) also find that the CMB has negligible influence on far infrared SEDs at $z < 10$. Therefore, the possible trend must arise from heating of dust by young stars within the galaxies and be associated with differences in the stellar populations and/or the ISM at high redshift compared with local galaxies.

The general trend toward higher SED temperature with redshift indicates an increase from typical temperatures of ~ 24 K at $z = 0$ to ~ 40 K at $z = 3.5 - 4$ and would predict $T \sim 51$ K at $z = 6$ (Schreiber et al. 2018). However, fits to the SEDs of high redshift quasar host galaxies indicate that in addition there is a much larger contribution in the rest $10 - 40 \mu\text{m}$ range from very warm dust than would be predicted just by shifting local templates toward higher temperature (Lyu et al. 2016). It is premature to try to model the far infrared SED behavior accurately *ab initio*; instead we focus on identifying a galaxy with a SED that can be used as a template for the high-redshift SEDs. To do so, we first discuss the available theoretical constraints. Section 2 of this paper shows that the very warm dust can be the result of the silicate-rich dust composition expected for galaxies $\lesssim 400$ Myr in age, particularly at the high UV radiation density of very high redshift galaxies. However, there is a large range of possible optical properties and resulting SEDs from such dust. It is not possible to sort out the “best” model for the silicate rich dust of the eight we consider, so we need to appeal to a real galaxy with conditions as close as possible to those expected for the high redshift galaxies. In Section 3 we show that conditions in Haro 11 match reasonably well those in luminous infrared galaxies at $z \sim 6$, including having an environment conducive to its dust being silicate-rich. However, all of the silicate-rich compositions predict SEDs that are weak in the far infrared (at $\sim 100 \mu\text{m}$) compared with the SED of Haro 11. We show that addition of a small amount of amorphous carbon dust to the silicate-rich dust in the theoretical models removes this discrepancy. The addition of this carbon is consistent with some models of star formation in the early Universe, and is also required by the detection of the $158 \mu\text{m}$ carbon line in a number of $z \sim 6$ galaxies (e.g., Pentericci et al. 2016; Bradac et al. 2017; Decarli et al. 2017; Smit et al. 2018). We therefore adopt the SED of Haro 11 as an empirical template for comparison with the measurements of high redshift galaxies. This comparison is carried out in Section 4, where we show that this template is a better fit to the data at $z > 5$ than any of the other proposed possibilities. Understanding FIR SEDs at high redshift is important to calculate total luminosities and to calibrate determinations of star formation rates (SFRs). Section 5

discusses how the selection of a Haro-11-based template affects luminosities from the existing database of Herschel measurements. Additional future determinations will largely utilize continuum measurements with the Atacama Large Millimeter/submillimeter Array (ALMA). Most of the observations with ALMA are made at about 1 mm, so we also discuss the template-dependence of the deduced luminosity from such data. The major results of the paper are summarized in Section 6.

2. MODELING THE FAR INFRARED SEDS OF HIGH REDSHIFT GALAXIES

2.1. General Behavior of Population II Galaxies

Our SED models in the FIR are based on those developed for primeval galaxies⁵ by De Rossi & Bromm (2017), hereafter DB17. According to their findings, the FIR SEDs of these galaxies are likely to be significantly warmer than typical FIR SEDs of galaxies in the $0 < z < 3$ range. Our goal is to explore this transition between $z = 3$ and $z \sim 10$. Such behavior likely arises in large part because of the high energy density in young Pop II galaxies combined with the characteristics of the silicate-rich dust expected in systems that are dominated by Pop III enrichment. Silicates have relatively poor emission efficiency at wavelengths short of about $8 \mu\text{m}$ and longer than about $60 \mu\text{m}$ (Koike et al. 2003), accentuating the tendency from the high energy density for relatively high temperatures for the dust. *The transition in FIR SEDs may therefore depend not on the transition from Pop III to Pop II in itself, or on the duration of the Pop II burst of star formation, but directly on the transition away from silicate-rich dust.* We will adapt the model of DB17 to conditions in the galaxies being detected in the far infrared at redshifts of $z \sim 6$ to explore this possibility.

The composition of Pop III dust is not well known (e.g., Schneider et al. 2016; Jaacks et al. 2018). As a specific example, Ji et al. (2014) considered silicon-based dust models taken from Cherchneff & Dwek (2010), and DB17 calculated the FIR SEDs for these different models. It is worth mentioning that, for estimating dust chemical composition, Cherchneff & Dwek (2010) assumed non-equilibrium chemical kinetics for dust formation, while most steady-state models would predict a more significant carbon composition. The suppression of carbon in the former case is related to the hypothesis that carbon-rich regions in the supernova ejecta are microscopically mixed with helium ions. As in DB17, we follow these assumptions to probe how silicate-rich dust from Pop III/II stars can affect the infrared SED; we will return to the issue of carbon dust in Section 3.

⁵ We use the following terminology: (1) Population III (Pop III) stellar systems contain metal-free stars that begin the enrichment of their ISMs through type II supernovae; and (2) Population II (Pop II) galaxies are the descendants of Pop III stellar systems with metal-poor stars that continue to enrich the ISM through an increasing variety of processes as they evolve. An extreme case within the latter category are “one-shot” systems where the metal enrichment reflects pure Pop III nucleosynthesis (Frebel & Bromm 2012). However, the exact duration of the intense star forming episode in Pop II galaxies is not well-constrained; a plausible range is 0.1 - 0.5 Gyr (e.g., Kriek et al. 2016). In this paper, we focus on the period up to ~ 400 Myr past the initial formation of stars, representing the primeval galaxy stage, during which stars less massive than $3.5 M_{\odot}$ have not ejected significant amounts of carbon-enriched material into the ISM.

By analyzing the different dust chemical models implemented in Ji et al. (2014), DB17 found that, for galaxies with similar properties, the FIR intensities and general shapes of the predicted SEDs are similar, but the detailed spectral features show differences. As a result, the theoretical results can only be taken as representative; alternative mixtures of silicate-rich dust would alter the predicted SEDs, although the overall shape will remain controlled by the poor emission efficiency of this type of mineral outside the $8\ \mu\text{m}$ to $60\ \mu\text{m}$ range. Improving the correspondence between the predicted and an observed SED would require adjustments in the adopted silicate material that would have to be *ad hoc* in nature, given the lack of any other meaningful observational constraints.

Rather than attempting such adjustments, in the following section we will propose the galaxy Haro 11 as a kind of analog computer that can utilize empirically determined dust optical properties. As we discuss below, Haro 11 has an exceptionally high rate of star formation in a low-mass and (at least prior to the ongoing starburst) low metallicity galaxy. These conditions are conducive to its interstellar dust being dominated by the outputs of very young and massive stars, as is the case for the high redshift galaxies. The energy density in the dominant star forming region in this galaxy is also similar to that in the high redshift galaxies. We will show that the FIR SED of this galaxy generally resembles that predicted by the theoretical model. Lyu et al. (2016) have also suggested that the Haro 11 SED is a good match to the FIR SEDs of quasar host galaxies at $z \sim 6$. We will therefore adopt its SED as a proxy for the theoretical one and use it in the remainder of the paper to compare with far infrared observations of high redshift galaxies.

2.2. Conditions in the Modeled Galaxies

2.2.1. Dust Composition

Gas that is only enriched by Pop III nucleosynthesis will have a unique chemical signature that will be erased as the galaxy evolves to Pop II (Ji et al. 2015), most notably when stars with masses $< 3.5\ M_{\odot}$ enter the asymptotic giant branch (AGB) phase and yield large amounts of carbon. The calculations of DB17 hence assumed a silicate-rich dust composition (e.g., Ji et al. 2014; Marassi et al. 2015) produced by the type II supernovae that dominate the dust production in Pop III stellar systems (Di Criscienzo et al. 2014). The type II supernovae are also likely to be a significant source of dust in very young galaxies that evolve from Pop III (e.g., Asano et al. 2011; Ji et al. 2015). AGB stars will be another potential dust source in Pop II. Ventura et al. (2012a,b) find that low-metallicity massive AGB stars produce silicate-rich dust, while less massive ones produce substantial carbon, with the transition mass at $3.5\ M_{\odot}$. There may also be an additional less-abundant component of corundum/alumina (Ventura et al. 2014; Dell’Agli et al. 2014) from massive AGB stars. These theoretical predictions are confirmed observationally, e.g. by Ventura et al. (2015). A star of $3.5\ M_{\odot}$ has a main sequence lifetime of ~ 400 Myr, suggesting that the silicate-rich dust composition should dominate in galaxies younger than this age. This transition is likely to be more critical to the FIR output of a galaxy than the end of the Pop III stage of evolution.

Michalowski et al. (2011) and Michalowski (2015) find that the dust produced directly in AGB stars and type II supernovae may be insufficient to explain the amounts of dust found in high redshift galaxies, and that much of the dust must form in the ISM. However, this process is likely to be delayed past the timescale of interest for this paper - i.e., before significant carbon is injected into the ISM (Asano et al. 2011).

2.2.2. Sizes and SFR Surface Densities

To be detectable at current limits, individual high-redshift galaxies must have very high FIR luminosities. The median for those in our study at $5 \leq z < 7$ is $5.3 \times 10^{13}\ L_{\odot}$ (Section 3.2), which becomes $\gtrsim 10^{13}\ L_{\odot}$ even allowing for the median level of lensing amplification (Spilker et al. 2016). The latter luminosity indicates a SFR $\gtrsim 1000\ M_{\odot}\ \text{yr}^{-1}$, assuming a typical local initial mass function. The star forming regions in these galaxies are also compact (Spilker et al. 2016). Specific examples are sizes of 2.5×1.1 kpc at $\lambda_{\text{rest}} \sim 160\ \mu\text{m}$ for AzTEC3 with a SFR of $1100\ M_{\odot}\ \text{yr}^{-1}$ (Riechers et al. 2014), 1.8×1.3 kpc and 2.1×0.9 kpc at $\lambda_{\text{rest}} \sim 130\ \mu\text{m}$ for the two components of ADFS-27 with a combined SFR of $2400\ M_{\odot}\ \text{yr}^{-1}$ (Riechers et al. 2017), and 1.22 kpc and $4500\ M_{\odot}\ \text{yr}^{-1}$ also at $\lambda_{\text{rest}} \sim 130\ \mu\text{m}$ for SPT 0346-52 (Ma et al. 2016). The quasar host galaxies must also be very compact, given the difficulty in imaging them from underneath the glare of the quasar (e.g., Hutchings 2003, 2005; McLeod & Bechtold 2009; Targett et al. 2012; Mechtley et al. 2012). In fact, the dust continuum and [C II] emission of quasar host galaxies at $z \gtrsim 6$ typically have sizes of $\sim 1\text{--}3$ kpc (diameter) as revealed by ALMA (e.g., Wang et al. 2013; Decarli et al. 2018). Typical SFRs for these sources are $1000\text{--}5000\ M_{\odot}\ \text{yr}^{-1}$ (Lyu et al. 2016), presumably unlensed. These values suggest SFR surface densities of $300\text{--}2000\ M_{\odot}/(\text{yr}\ \text{kpc}^2)$. Under a broad range of conditions, the high luminosity density that results will produce a warmer FIR SED than would be found in lower luminosity density sources, such as normal nearby star forming galaxies (e.g., Chakrabarti & McKee 2005; Hayward et al. 2011).

2.2.3. Metallicity

Comparison of the recent rest-frame UV spectroscopic observations and optical broad-band photometry with photoionization models indicates metallicities of $Z = 0.0016\text{--}0.0026$ for a small sample of galaxies at $z > 6$ (Stark et al. 2017; Mainali et al. 2017), which is equivalent to $0.10\text{--}0.17\ Z_{\odot}$ (assuming $Z_{\odot} = 0.015$, Bressan et al. 2012). Moreover, Hashimoto et al. (2017) find that low metallicities ($< 0.02\ Z_{\odot}$) and young stellar ages (< 100 Myr) are a possible cause of the large Lyman- α equivalent widths of Lyman- α emitters at $z \sim 3\text{--}5$, which are representative of galaxies in the early stages of their evolution. However, these large equivalent widths can also be explained by anisotropic radiative transfer effects, fluorescence by hidden AGN or QSO activity, and/or gravitational cooling. Recently, comparison of hydrodynamical simulations with ALMA observations of CR7, a luminous Ly- α emitter at $z = 6.6$, suggests metallicities of $Z = 0.1\text{--}0.2\ Z_{\odot}$ for the star-forming clumps in this galaxy (Matthee et al. 2017). As a summary, based on the current observations, the metallicity of massive

star-forming galaxies at $5 \lesssim z \lesssim 7$ is estimated to be $\sim 0.1 - 0.2 Z_{\odot}$. Lower metallicities are, of course, expected for lower-mass galaxies and at higher redshifts (Bromm & Yoshida 2011). Future observations, e.g. with the *James Webb Space Telescope (JWST)*, are required to constrain the gas-phase metallicity of these high redshift galaxies better.

2.3. Modeling the Galaxy Far Infrared SEDs

The calculations of FIR SEDs by DB17 were for primeval galaxies dominated by Pop II stars, and assumed extremely low metallicities and compact star forming complexes. Figure 1 shows the result of further developing their model in circumstances more applicable to the very luminous galaxies detectable at very high redshift, as described in Section 2.1. To increase the far infrared outputs by 2 – 3 orders of magnitude to match the high luminosities of the galaxies, we (1) increased the virial masses (M_{vir}) of the modeled sources, (2) increased the gas metallicity to 1/3 that of the sun, and (3) assigned a dust-to-metal ratio of 0.02. In particular, the SEDs associated with different luminosities in Figure 1 correspond to sources with halo mass $M_{\text{vir}} = 10^{10}, 10^{11}, 10^{12}$ and $10^{13} M_{\odot}$. As in DB17, the stellar mass fraction is set to $f_* = M_*/(M_* + M_{\text{gas}}) = 0.01$.

We evaluated eight of the sets of dust optical constants from Ji et al. (2014) to sample the resulting variations in the SEDs; to suppress sharp features we smoothed the optical constants with a logarithmic full width at half maximum of 0.075 (i.e., a factor of 1.19). Specifically for Figure 1 we used the dust composition UM-D-20 (see table 1 in Ji et al. 2014), which is silicate-rich with some alumina, and the “standard” size distribution from Ji et al. (2014). As we will show, the implementation of other silicon-based dust chemistries generally predicts similar shapes of the SEDs, but the detailed features exhibit some variations. The use of other size distributions for the dust grains can lead to moderate variations in the total luminosities, with the exact value depending on the dust chemical composition. As discussed in Ji et al. (2014), a variety of dust compositions and size distributions are possible; our calculations are illustrative of the far infrared SEDs that might be expected from very young galaxies, but the detailed spectral features are a product of the specific grain composition assumed and should not be taken to be unique. For further details regarding these choices, we refer the reader to DB17.

The models assume that the galaxy size is given by the virial radius. This has the effect that within a given family of models, such as those displayed in Fig. 1, the mass-density is similar, independent of luminosity. The luminosity density exhibits a modest dependence, increasing by an order of magnitude over the range of luminosities in Fig. 1. As shown by DB17, moderate changes in the gas-phase and dust density profiles (at a fixed mass) would not generate significant changes in the SEDs, but an increase of the dust-to-metal ratio or gas-phase metallicity drives an almost proportional increase of emission by dust without substantially changing the shape of the SED.

Figure 2 demonstrates how different assumptions affect the SEDs. All four SEDs in this figure are for a luminosity of $\sim 4 \times 10^{10} L_{\odot}$. In particular, we analyze the effects of extending the heating source by distribut-

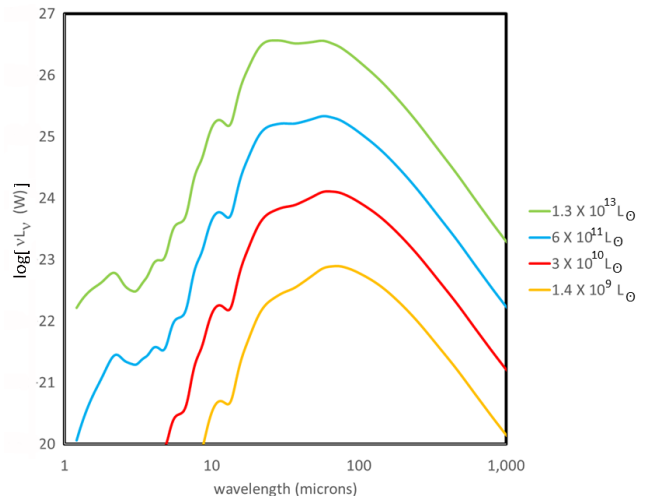


FIG. 1.— Predicted far infrared SEDs for the modeled galaxies, as a function of their total infrared ($5 - 1000 \mu\text{m}$) luminosities. The models are based on those discussed by DB17 with stellar mass fraction (f_*) of $M_*/(M_* + M_{\text{gas}}) = 0.01$, modified to set the gas-phase metallicity to $0.33 Z_{\odot}$, and dust-to-metal ratio to 0.02. The detectable galaxies at $z > 5$ have luminosities $\gtrsim 10^{13} L_{\odot}$, similar to the most luminous case illustrated. For the sake of clarity, only SEDs from the UM-D-20 model are shown.

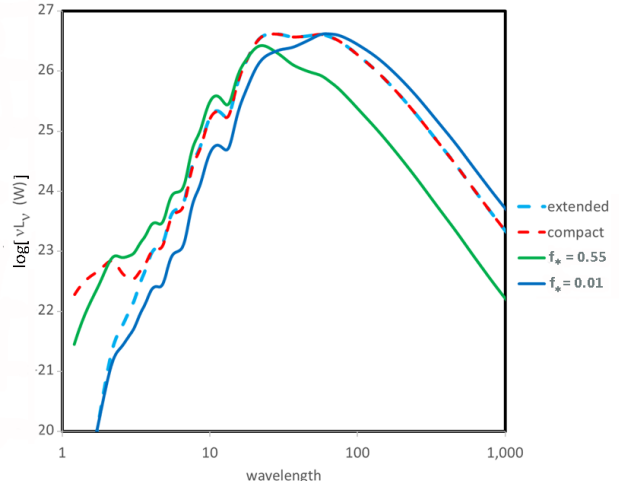


FIG. 2.— Examples of changes in the theoretical SED with changes in the distribution of heating sources and in the luminosity density, expressed in terms of the stellar mass fraction (f_*). The model for compact heating assumes a single, central luminosity source, while the extended heating arises from sources randomly distributed within a 100 pc radius. The luminosity density increases by an order of magnitude between $f_* = 0.01$ and $f_* = 0.55$.

ing individual stellar groups over a radius of 100 pc. The cases for an extended star cluster vs. a single central source merge for wavelengths $> 5 \mu\text{m}$, so the distribution of heating sources to first order has relatively little effect on the predicted mid- and far-infrared SED. The increase in stellar mass fraction (sometimes called star formation efficiency) is accompanied by a decrease in the virial radius by a factor of 0.45, so there is an increase by an order of magnitude in the luminosity density that manifests itself as a modestly “bluer” SED, shifted to shorter wavelengths by a factor of about two. Thus, the far infrared SED changes with increasing luminosity density, but not dramatically. These results show that the

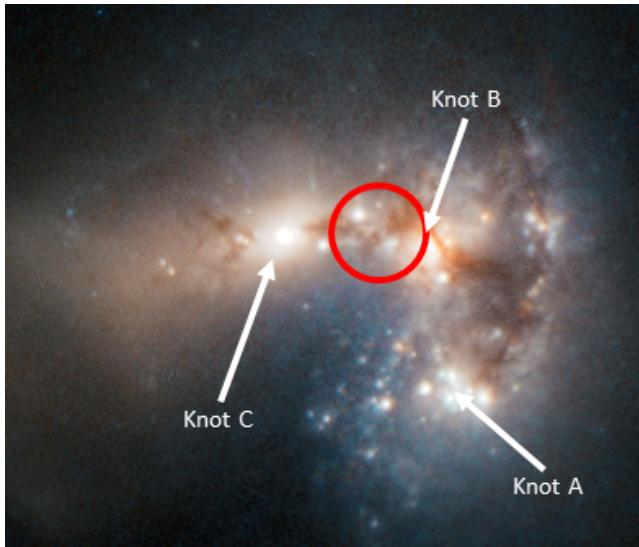


FIG. 3.— Image of Haro 11 from Adamo et al. (2010). The red circle ($2''$ in diameter, or 700 pc) shows the location of the $24\ \mu\text{m}$ source and its diameter is roughly the upper limit on the size that can produce the majority of its signal, as implied by the diffraction-limited *Spitzer* image (Lyu et al. 2016). Credit: ESA/Hubble/ESO and NASA.

emission efficiency of the silicate-rich dust has a strong influence on the FIR SED, making it relatively insensitive to changes in the architecture of the galaxy.

3. COMPARISON WITH SED OF HARO 11

3.1. Conditions in Haro 11 compared with those in high redshift galaxies

We now consider why Haro 11 is a useful analog to luminous, high redshift galaxies. The visible image of Haro 11 is complex with three bright knots (A, B, and C) within a fainter surrounding, the general appearance of a complex merging system, and with a rich population of very young super star clusters (e.g., Adamo et al. 2010). However, the very luminous infrared emission is compact and centered on Knot B (e.g., Lyu et al. 2016; Chu et al. 2017); see Figure 3, and indicates a SFR of about $30\ M_{\odot}\ \text{yr}^{-1}$ from this knot (Lyu et al. 2016). This knot has a higher metallicity than the rest of the galaxy (James et al. 2013), consistent with it being a site dominated by this ongoing starburst. Knot B has a radius of about 140 pc and a mass of about $2 \times 10^9\ M_{\odot}$, determined dynamically (Östlin et al. 2015). Its specific star formation rate is thus $\sim 15\ \text{Gyr}^{-1}$ and its SFR surface density is $\sim 500\ M_{\odot}\ \text{yr}^{-1}\ \text{kpc}^{-2}$; both values are typical of luminous high redshift galaxies.

The stellar population powering the far infrared emission appears to be very young, with a typical age of only 3.5 Myr (Adamo et al. 2010). A rough estimate of the total mass of very young stars is $3 \times 10^8\ M_{\odot}$, obtained by assuming the current level of SFR for 10^7 years. A substantial fraction of the mass in Haro 11 arises from cold gas, which from its radial velocity resides primarily in Knot B (Cormier et al. 2014). Indeed, if the gas mass is estimated from the far infrared emission, it accounts for most of the dynamical mass of $2 \times 10^9\ M_{\odot}$ (Östlin et al. 2015). Hence, the newly formed stars could be responsible for a very substantial fraction of the total stellar mass in Knot B; it is a region that is potentially young-star-

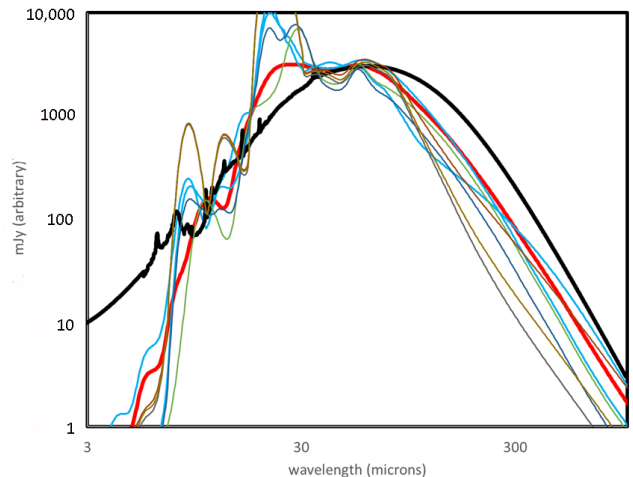


FIG. 4.— Comparison of the FIR SED of the model from Fig. 1 and 2 for a galaxy of $1.3 \times 10^{13}\ L_{\odot}$ (thick red line) with that of Haro 11 (black). Seven alternative models using different possible optical constants (U-M-20, U-M-170, UM-D-170, M-ND-20, M-ND-170, UM-ND-20, UM-ND-170; see Ji et al. 2014, for details) are also shown in finer lines.

dominated and hence a candidate to have silicate-rich dust.

The oxygen abundance in Knot B is cited nominally as $12 + \log(\text{O}/\text{H}) = 8.33 \pm 0.01$, where the quoted error does not allow for systematic errors (Guseva et al. 2012), or 8.25 ± 0.15 (James et al. 2013), values that are $\sim 36 - 44\%$ of solar⁶. This abundance is a factor of about three greater than our estimate for the high redshift ($z \sim 6$) galaxies. The aromatic bands are very weak (Wu et al. 2006), consistent with a carbon-poor ISM. However, other explanations are possible since the excitation and destruction of the aromatic bands is a complex and not well-understood process.

In summary, the analogy of expected conditions in Haro 11 with those in luminous infrared galaxies at $z \sim 6$ is reasonably good.

3.2. Comparison of Haro 11 SED with theoretical models

In Figure 4, we compare the SEDs from our theoretical models with that for Haro 11 (from Lyu et al. 2016, and references therein). As discussed previously, the model is conceptual - the lack of detailed information about the optical constants for the dust in silicate-rich galaxies means that the details of the SED are not significant. Nonetheless, some important trends are evident. First, the models do reflect the warmer temperature of Haro 11 reasonably well, and they *all* show the strong emission in the $10 - 40\ \mu\text{m}$ range, characteristic of the very warm dust that is also seen in the high redshift galaxies. The detailed behavior in this spectral range differs substantially from one set of optical constants to another. Even with much better constraints on the optical constants, a broad variety of behavior is also seen in spectra of local low metallicity galaxies where the silicate bands appear anywhere from strong emission to absorption (Rémy-Ruyer et al. 2015). For these local galaxies, despite the complete sets of observations, modeling the silicate bands in a general way is still challenging; Rémy-

⁶ taking the solar $12 + \log(\text{O}/\text{H}) = 8.69$

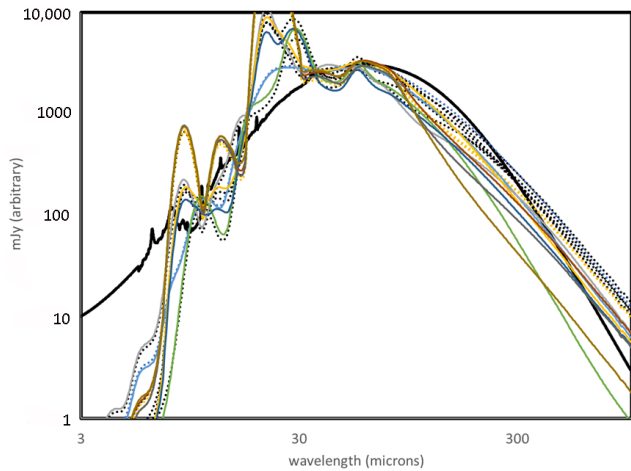


FIG. 5.— The effect of adding emission from amorphous carbon dust to the eight types of silicate rich dust from Ji et al. (2014). The solid lines show the results if 10% of the luminosity is from the carbon dust and the dotted lines show the results for 20% coming from the carbon. The thick black line is the SED of Haro 11.

Ruyer et al. (2015) had to introduce an additional spectral feature in the form of a warm modified blackbody to improve the fits to their observations. The selection of the appropriate optical constants among the possibilities for Pop III/II galaxies and detailed modeling of their spectra such as that for local galaxies by Rémy-Ruyer et al. (2015) is beyond the scope of this paper.

However, the deficiency in output at wavelengths $> 100 \mu\text{m}$ relative to the behavior of Haro 11, present in all models, needs to be addressed. There is ongoing discussion of whether there is a modest amount of carbon dust in the earliest galaxies (e.g., Nozawa & Kozasa 2013; Marassi et al. 2015). In any case, the detection of the [CII] $158 \mu\text{m}$ line in galaxies at $z > 5$ (e.g., Pentericci et al. 2016; Bradac et al. 2017; Decarli et al. 2017; Smit et al. 2018) demonstrates that there is some level of this element in typical ISMs at this redshift, indicating also the presence of carbon dust. We therefore computed the infrared SED expected for amorphous carbon, using optical constants from Karl Misselt (private communication), based on those of Zubko et al. (1996). It is not possible to determine the abundance of carbon in these galaxies accurately from the $158 \mu\text{m}$ line detections (Lagache et al. 2018). In addition, the emission efficiency of carbon depends strongly on its form (e.g., amorphous or graphite, see Rémy-Ruyer et al. (2015)), so we do not show results as a function of relative densities of carbon and silicate dust. Instead, in Fig. 5 we show the eight silicate-rich models considered in Fig. 4, but with 10% and 20% of the total luminosity contributed by carbon. It appears that the addition of a small amount of carbon dust can substantially improve the correspondence of the silicate-rich templates to the SED of Haro 11.

Given the correspondence of the SED of Haro 11 to the model predictions, we adopt the Haro 11 SED as a proxy template to study the observed behavior of FIR SEDs with redshift. We provide the Haro 11 SED in electronic form in Appendix A.

4. EMPIRICAL CONSTRAINTS ON THE HIGH REDSHIFT FAR INFRARED SEDS

The preceding section has demonstrated the theoretical expectation that the SEDs will be relatively “warm”

and broad for galaxies where: (1) a very recent episode ($< 400 \text{ Myr}$ old) of star formation dominates the composition of the interstellar dust; and (2) the galaxy luminosity and size are appropriate for young galaxies at high redshift. We now compare far infrared and sub-mm measurements of galaxies at $2 \leq z < 7$ with this prediction. We begin with the range $2 \leq z < 4$ (median infrared luminosity of $6 \times 10^{12} L_{\odot}$ for $z = 2 - 3$ and $1.8 \times 10^{13} L_{\odot}$ for $z = 3 - 4$), demonstrating that the appropriate template derived from local luminous infrared galaxies provides a good fit to all the available far infrared/sub-mm observations. We next consider the range $5 \leq z < 7$ (median infrared luminosity $5.3 \times 10^{13} L_{\odot}$), finding that the Haro 11-based template is the better fit. Finally, we consider the $4 \leq z < 5$ range (median infrared luminosity $3.2 \times 10^{13} L_{\odot}$), finding that it shows hints of a transition from the lower redshift template to the Haro 11 one, i.e., it provides a bridge between the former cases. The quoted median luminosities are apparent, not allowing for lensing; it is expected that many of these sources are in fact lensed (Strandet et al. 2016), with typical amplifications of ~ 6 (Spilker et al. 2016). Nonetheless, the changes we see in the far infrared SED are very different from the changes in local templates with increasing luminosity where, for example, the far infrared peak narrows (Rieke et al. 2009), so we believe that the unavoidable increase in detectable apparent luminosity with redshift cannot account for the change in SEDs.

4.1. Far Infrared SEDs at $z \sim 3$

At redshifts of 1 – 3, Rujopakarn et al. (2013) found that star formation rates estimated from rest-frame $24 \mu\text{m}$ photometry on the basis of templates from Rieke et al. (2009) for $\log(L(\text{TIR})) = 11.25 - 11.75$ gave reasonably accurate results⁷ for all galaxies with infrared luminosities above $\sim 10^{11} L_{\odot}$. This conclusion indicates that these templates are a reasonably accurate representation of the FIR SED of these galaxies. We start with this result to provide the fiducial SED against which we will study the evolution with increasing redshift toward a FIR SED resembling more closely that of Haro 11.

In general, well-sampled far infrared SEDs are not available at very high redshifts, so our method is to collect all cases where there are measurements of reasonably high signal to noise covering a sufficient wavelength range to be useful in constraining the shape of the far infrared SED. We also require spectroscopic redshifts to avoid artificially broadening the SED due to redshift errors. Table 1 lists the galaxies and the sources for the measurements we have used. Most of the galaxies are selected at long wavelengths, although in the rest frame there are many examples bridging the peak of the FIR SED. Specifically, Wang et al. (2016) select at $160 \mu\text{m}$, Casey et al. (2012a) at $250 - 500 \mu\text{m}$, Shu et al. (2016) at $500 \mu\text{m}$, and the remaining cases in this redshift range are selected in the mm-range.

We shift the measurements to the rest frame and normalize them to the same value (relative to the assumed template) near the peak. This normalization uses χ^2 minimization to the template between rest wavelengths

⁷ Kirkpatrick et al. (2015) derived a similar template using a different technique, fitting the photometry of multiple galaxies over a range of redshifts.

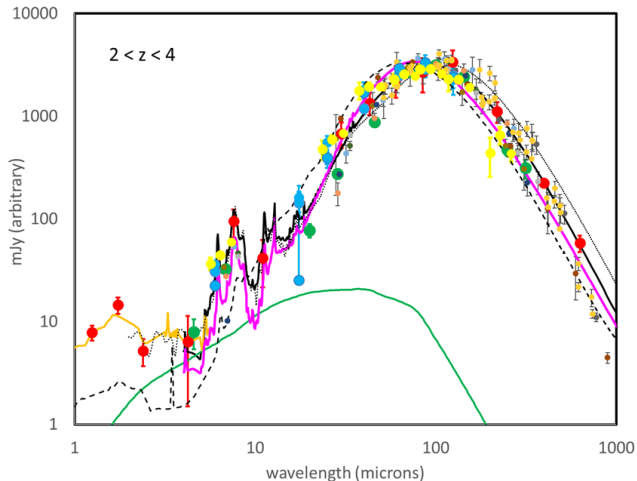


FIG. 6.— Templates and data for infrared galaxies at $2 < z < 4$. The solid black line is the template for $\log(L(\text{TIR})) = 11.25$ and the purple line for $\log(L(\text{TIR})) = 11.75$ from Rieke et al. (2009), and represent the range of these templates recommended at high redshift by Rujopakarn et al. (2013). The large red points are for the combined *Spitzer* + *Herschel* + ALMA photometry from Dunlop et al. (2017), median $z = 2$. They have been fitted at the shortest wavelengths by a stellar SED (orange) normalized to optimize the fit, and a “normal” quasar SED (green) (Lyu & Rieke 2017a) has been subtracted. The large green points are from Wang et al. (2016), JH-red SF HIEROS; they have a median $z = 2.5$. The large yellow points are from Béthermin et al. (2015) for stacked data in the COSMOS field. The large blue points are for the stacked results in the CANDELS fields from Schreiber et al. (2018) for $2.5 < z < 3.5$; all three mass ranges are shown because the differences are minimal. The other (small) points are for individual galaxies, listed in Table 1. The dashed line is the template for $1 \times 10^{13} L_{\odot}$ from Chary & Elbaz (2001) and the dotted one is the SFG2 template from Kirkpatrick et al. (2015). The template for $z = 3$ from Schreiber et al. (2018) is not plotted for clarity; it falls very close to the Rieke et al. (2009) $\log(L(\text{TIR})) = 11.25$ one for $\lambda < 100 \mu\text{m}$ and the $\log(L(\text{TIR})) = 12.25$ one (Rieke et al. 2009) (not shown here), for $\lambda > 100 \mu\text{m}$. The template from Magdis et al. (2012) is also not plotted; it falls close to the Rieke et al. (2009) $\log(L(\text{TIR})) = 11.25$ one.

of 50 and 200 μm , i.e. χ^2 is minimized using all the measurements that fall within this spectral range. To support this step, we require at least three measurements with signal to noise ratios > 3 in this spectral range. Since this range covers the peak of the SED, the normalization is roughly by far infrared luminosity. The normalization depends only on the peak of the FIR SED, so it leaves the measurements at shorter and longer wavelengths to characterize the SED shape.

Figure 6 shows the result for $2 \leq z < 4$, along with the $\log(L(\text{TIR})) = 11.25$ and 11.75 templates (Rieke et al. 2009), as well as templates from Chary & Elbaz (2001) and Kirkpatrick et al. (2015). Some of the points are from combinations of data for a number of galaxies. The composite data points from Dunlop et al. (2017) are based on galaxies detected in a deep ALMA map of the Hubble Ultra-Deep Field. The red HIEROS from Wang et al. (2016) are massive, dusty, star forming galaxies at redshifts of 2–3 (plus passive galaxies at higher redshifts that will not contribute to the far infrared); the median redshift of these galaxies is $z = 2.5$ and the quoted errors are about the same size as the points. Béthermin et al. (2015) present stacked measurements in the COSMOS field; we show results from the bins between $z = 2$ and $z = 3.5$. Schreiber et al. (2018) stacked *Herschel* measurements of galaxies in the CANDELS fields; we show

the results for $2.5 < z < 3.5$. The remaining points are for individual galaxies.

The values of χ^2 provide a quantitative evaluation of the validity of the templates. A few measurements have very high ratios of nominal signal to noise, up to 20:1. To allow for effects such as confusion noise and at the same time to keep one or two measurements from dominating the results, we added a uniform additional noise of 15% of the measured total flux density value for the individual galaxies and 7.5% for the stacked results, in quadrature with the quoted noise. We also reject the 5 most discordant measurements (out of a total of 163), and evaluate the templates only between 11 and 700 μm . The $\log(L(\text{TIR})) = 11.25$ template yields $\chi_{\text{red}}^2 = 1.87$. The agreement is significantly worse with the $\log(L(\text{TIR})) = 11.75$ template ($\chi_{\text{red}}^2 = 2.91$) and with the Chary & Elbaz ($\chi_{\text{red}}^2 = 5.61$), Kirkpatrick ($\chi_{\text{red}}^2 = 4.06$), and Schreiber ($\chi_{\text{red}}^2 = 3.05$) ones. The Magdis et al. (2012) $z = 2.5$ template is also somewhat worse, $\chi_{\text{red}}^2 = 2.27$. These values of χ_{red}^2 could be reduced by assigning a value larger than 15% to the additional noise, but we have not done that because there are likely to be intrinsic variations among the galaxies relative to a single template, and they will contribute to the scatter. We will use the $\log(L(\text{TIR})) = 11.25$ template as the standard of comparison in the following sections to demonstrate any systematic changes. However, it appears to overestimate the strength of the aromatic bands modestly, consistent with the finding of Rujopakarn et al. (2013) that the rest $\sim 8 \mu\text{m}$ fluxes require templates with $\log(L(\text{TIR})) = 11.25 - 11.75$ for good fits. Since this paper is focused on wavelengths $\geq 11 \mu\text{m}$, this is not an issue.

4.2. Far Infrared SEDs at Higher Redshift

We now apply a similar approach to luminous infrared galaxies at $5 < z < 7$. The measurements of individual galaxies with adequate far infrared observations are listed in Table 1. We also used measurements of six quasars with adequate signal to noise *Herschel* FIR measurements and a large excess attributed to their host galaxies, namely J0338+0021, J0756+4104, J0927+2001, J1202-3235, J1204-0021, and J1340+2813; flux densities and redshifts were taken from Leipski et al. (2014). We subtracted the quasar contribution using the “normal” quasar template (Xu et al. 2015), as opposed to dust-deficient quasar templates (see Lyu & Rieke 2017a), to derive the SEDs of the host galaxies. None of the fits in Lyu et al. (2016) would ascribe a significant fraction of the FIR emission to the quasar, a conclusion that is confirmed by arguments in Appendix B.

To look for changes in far infrared SEDs between $z \approx 3$ and 6, in Figure 7(a) we compare all of the available measurements with adequate signal to noise at the latter redshift to the local $\log(L(\text{TIR})) = 11.25$ template that gave the best fit for $2 < z < 4$. The correspondence is poor, largely because the SED is too cool. The poor fit would also apply to the approach of Magdis et al. (2012), whose template resembles the $\log(L(\text{TIR})) = 11.25$ one, and who argue for little SED evolution at $z > 3$. The local $\log(L(\text{TIR})) = 12.25$ template has a warmer SED, but nonetheless it has significant divergence at both short and long wavelengths. Schreiber et al. (2018) extrapolate the temperature relation derived for $z < 4$ to deduce an

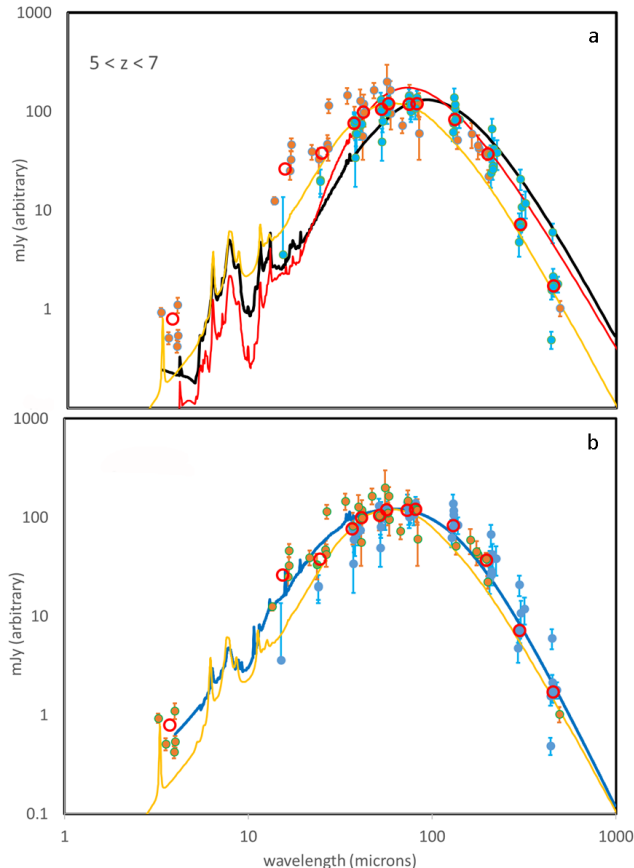


FIG. 7.— (a) Measurements of galaxies at $5 < z < 7$, shifted to the rest frame and compared with the $\log(L(\text{TIR})) = 11.25$ (black) & 12.25 (red) templates from Rieke et al. (2009), plus the $z = 6$ template from Schreiber et al. (2018) (orange). The deep orange points are for the quasar host galaxies and the blue ones for galaxies not selected for AGN. Medians in groups of 5 - 11 measurements at adjacent wavelengths are shown as red circles. The χ_{red}^2 for the $\log(L(\text{TIR})) = 11.25$ fit is 6.1, for $\log(L(\text{TIR})) = 12.25$ it is 4.5, and for the Schreiber template it is 3.25 (see text for details). The points at $\lambda < 5.5 \mu\text{m}$ may have significant contributions by direct stellar emission and should not be considered as part of the far infrared SED. The measurements suggest that these templates are all significantly too narrow at this redshift range. (b) Measurements as in (a), compared with the SED of Haro 11 (dark blue line). The χ_{red}^2 for the fit is 1.57 (see text for details), indicating a much better fit than in (a).

SED at $z = 6$ with a temperature about 10 K warmer than at $z = 3.5$. Figure 7(a) shows their template for $z = 6$; the correspondence with the data is improved but still not fully satisfactory. To render these impressions quantitative, we follow the procedures in Section 4.1 to determine χ^2 for the templates in Figure 7(a). We found a χ_{red}^2 of 6.1 for the $\log(L(\text{TIR})) = 11.25$ template, 4.5 for the $\log(L(\text{TIR})) = 12.25$ one, and 3.25 for the one from Schreiber et al. (2018). None of them fits well because the SEDs are too narrow. The measurements indicate the need for a broader template.

Figure 8 is similar to Fig. 7, but for $4 \leq z < 5$. It appears that the SEDs at $z \approx 4.5$ are a bridge from the local templates to the broader one needed to fit the data at $z > 5$. Figure 7(b) shows the measurements in Fig. 7(a), fitted by the Haro 11 SED by χ^2 minimization, using the same procedures as in Section 4.1. The fit has a χ_{red}^2 of 1.57. There appears to be no system-

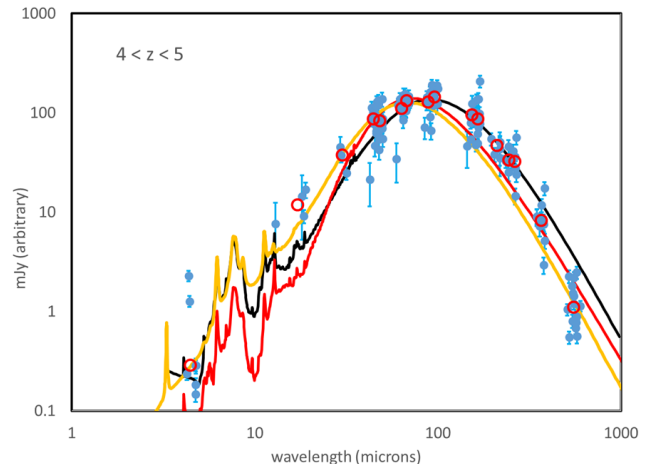


FIG. 8.— Measurements of galaxies at $4 < z < 5$, shifted to the rest frame and compared with the $\log(L(\text{TIR})) = 11.25$ (black) and 12.25 (red) templates from Rieke et al. (2009) and with that from Schreiber et al. (2018) for $z = 4.5$ (i.e., the average of those for $z = 4.4$ and 4.6). Medians of the measurements in groups of 3 - 12 measurements at adjacent wavelengths are shown as red circles.

atic difference between the points derived from quasar host galaxies and those from galaxies without luminous AGN. However, the points between 10 and $50 \mu\text{m}$ are mostly derived from the host galaxies because only they have useful measurements in the 100 and $160 \mu\text{m}$ Herschel bands. Appendix B demonstrates that it is very unlikely that these values are significantly contaminated by quasar emission. For comparison, we also show the relevant template from Schreiber et al. (2018). The Haro 11 SED is broader, and that results in a better fit to the measurements as indicated by its lower χ^2 , 1.57 vs. 3.25, when computed in identical ways. To convert the relative χ_{red}^2 values to probabilities, we increased the additional noise component from 15% to 22% of the measured flux, to set χ_{red}^2 for the Haro 11 template to 1. The probability to obtain by chance the resulting χ_{red}^2 for the Schreiber template, $\chi_{\text{red}}^2 = 2.10$, is then $\sim 10^{-8}$. This probability is reduced as the additional noise term is reduced from 22% toward 15%.

We conclude that the Haro 11 SED provides a significantly better template for galaxies at $z > 5$, compared with templates derived at lower redshift. Other than the quasar host galaxies, the galaxies in Fig. 7 are nearly all selected in the mm-waveband, corresponding to rest wavelengths around $150 \mu\text{m}$, which could produce a mild bias toward “cold” SEDs. Nonetheless, their SEDs are significantly brighter in the mid-infrared ($10 - 40 \mu\text{m}$) and hence “warmer” than is indicated by templates derived at lower redshift, as shown in Fig. 7.

The slope of the Haro 11 SED at wavelengths longer than $100 \mu\text{m}$ may be slightly steeper than those of other templates. To set an upper limit for the CMB contribution to the dust temperature, we estimated the emissivity index β (where the departure from gray emissivity goes as $\lambda^{-\beta}$) just for wavelengths $\geq 100 \mu\text{m}$, obtaining $\beta = 1.2$. A more conventional estimate gives $\beta \approx 1.9$ (Lyu et al. 2016), compared with values of 1.5 - 2.0 for typical high metallicity main sequence luminous galaxies (e.g., Elbaz et al. 2011; Magdis et al. 2012; da Cunha et al. 2013). Any differences in the sub-mm SEDs would be subtle, making it difficult to distinguish the two cases in

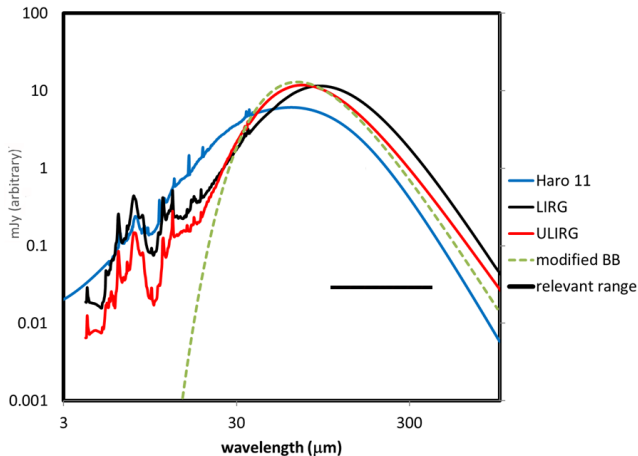


FIG. 9.— Influence of template selection on SFR estimates from ALMA measurements at ~ 1 mm. All of the templates have been normalized to the same total infrared luminosity. The modified blackbody is as in Wang et al. (2007, 2008); Leipski et al. (2014); Willott et al. (2013, 2017). The horizontal black bar shows the most relevant wavelength range (100–400 μm rest) for interpreting single-band measurements near $\lambda_{\text{observed}} \sim 1$ mm of galaxies at $z \sim 1 - 10$.

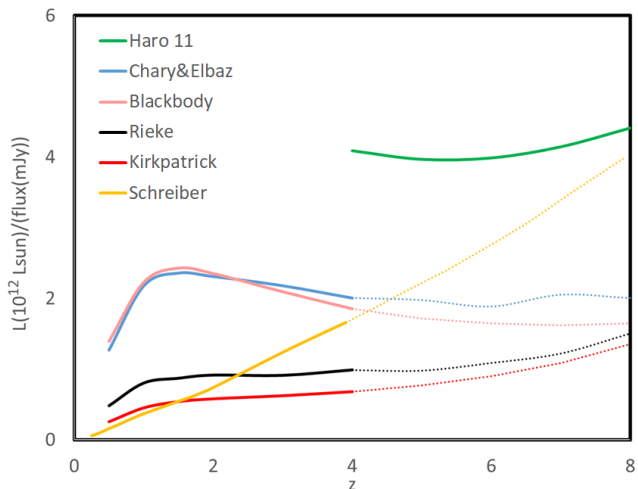


FIG. 10.— Conversion factors from ALMA observed Band 7 flux densities in mJy to $L(\text{TIR})$ in units of $10^{12} L_{\odot}$, for various SED templates. The conversions follow the approach of Schreiber et al. (2018); given a flux density in mJy, if it is multiplied by the appropriate conversion factor for the redshift of the galaxy, the result is in units of $10^{12} L_{\odot}$. The blackbody curve is for $T = 47$ K, $\beta = 1.6$, the Chary & Elbaz template is for $10^{13} L_{\odot}$, and the Kirkpatrick template is their SFG2 template. Beyond $z = 4$, all the templates except that based on Haro 11 are extrapolated, and hence are shown as dotted lines.

that spectral range. Therefore, this potential bias does not undermine the conclusion that the Haro 11 template is the better template to use at these redshifts.

Our results show that the SEDs of infrared galaxies continue to evolve toward warmer temperature going from $z \sim 3$ to $z \sim 6$, in agreement with the extrapolation in Schreiber et al. (2018), but contrary to the assumptions in Elbaz et al. (2011) and Magdis et al. (2012). The extent of the potential change in shape of the far infrared SEDs for $z \gtrsim 5$ is not anticipated in any previous sets of templates.

5. IMPLICATIONS FOR LUMINOSITY ESTIMATION

Spectral templates are central in determining average, or “typical,” properties of high-redshift galaxies. Perhaps the most critical use of them is determining total infrared luminosities, which for luminous, dust-shrouded galaxies provides an estimate of the luminosity in young and massive stars. Combined with the initial mass function, one can then obtain the star formation rate for a galaxy. Here we consider the impact of using the Haro 11 template on such estimates in two cases: (1) where Herschel measurements at 250 μm and longer wavelengths are available; and (2) when there is only a single-band measurement near 1 mm with ALMA.

5.1. Luminosities from Herschel measurements

The influence of template choice on the deduced far infrared luminosity with Herschel measurements is not uniquely determined; it depends on the bands measured and the method used to normalize the templates to the measurements (i.e., there is often an additional error term above the nominal measurement errors). For a specific example, however, we have assumed a galaxy at $z = 5, 6$, or 7 with measurements at 250, 350, and 500 μm (typical for such data on galaxies at $z \sim 6$) and equal weights. We then find that the luminosity deduced with the Rieke et al. (2009) LIRG and ULIRG templates and the Schreiber et al. (2018) one for $z = 5$ would all be about 77% lower than with the Haro 11 one. At $z = 6$, the results would be 99, 68, and 77 % of that from the Haro 11 template respectively. At $z = 7$ they are respectively 121, 79, and 82%. These values are only illustrative, given the differences that would result from different measurement weights.

5.2. Luminosities from single-band ALMA measurements

Single-band ALMA measurements near 1 mm are being used to estimate infrared luminosities and star formation rates at $z \approx 6$ (e.g., Wang et al. 2013; Willott et al. 2017; Decarli et al. 2018). One consequence of the far infrared SED derived here for high-redshift galaxies is that such an approach could systematically underestimate the total infrared luminosities and hence the SFRs. Figure 9 compares a number of relevant SEDs to illustrate the issue. The LIRG spectrum ($\log(L(\text{TIR}))=11.25$) has been shown to be typical of even the most luminous galaxies at $1 < z < 3$ (Rujopakarn et al. 2013, this paper). The modified black body ($T_d = 47$ K, $\beta = 1.6$) is commonly used to interpret the ALMA 1mm measurements (e.g., Wang et al. 2007, 2008; Leipski et al. 2014; Willott et al. 2013, 2017). The horizontal black line extends from 100 to 400 μm , roughly the relevant rest spectral range for the interpretation of the ALMA bands 6 and 7 results at $z \sim 1 - 10$. The various possible choices for the SED result in significant differences in the total infrared luminosities that would be deduced.

This issue is illustrated graphically in Figure 10, which shows the conversion from flux densities measured in ALMA Band 7 (870 μm) to galaxy luminosities in units of $10^{12} L_{\odot}$, as in Schreiber et al. (2018). The differences in the conversion factors for objects at $1 < z < 4$ can be understood from Figure 6, which compares the different templates with observed photometry and confirms that the Rieke et al. (2009) template is a good

overall fit to the available measurements at these redshifts. The Kirkpatrick et al. (2015) template agrees closely with the Rieke et al. (2009) template at wavelengths $< 100\mu\text{m}$, which account for much of the total IR luminosity, but is significantly brighter at longer wavelengths. Consequently, a given luminosity yields a larger signal at the long wavelengths probed by ALMA Band 7 over this range of redshift, corresponding to observed wavelengths of $400 - 170\mu\text{m}$. In other words, a given signal in mJy needs a smaller multiplication factor to be converted to the total infrared luminosity using the Kirkpatrick template compared with the Rieke one. In contrast, the template from Chary & Elbaz (2001) is higher at $\lambda < 100\mu\text{m}$ and lower at longer wavelengths compared to the Rieke et al. (2009) template, such that a given signal in Band 7 requires a substantially higher total infrared luminosity. As shown in Figure 9, the modified blackbody is also higher at $\lambda < 100\mu\text{m}$ and lower longward of this wavelength compared to the Rieke et al. (2009) template, resulting in a similar behavior. The differences between the Chary & Elbaz (2001) and Kirkpatrick et al. (2015) templates are a factor of 3 – 4 over this redshift range. The Schreiber et al. (2018) results are based on templates that evolve in shape with redshift, and hence the behavior differs from the rest. None of these templates are constrained by data at $z > 4$, so we show the results at higher redshifts as dotted lines.

At $z \sim 6$, the Haro 11 SED appears to be a better fit to the data than any of the templates derived at lower redshift, and total luminosities derived using it on the basis of ALMA Band 7 measurements will be a factor of 2 – 4 higher than those from the extrapolations of the other templates. At redshifts of $z \sim 4 - 5$, it is possible that there is a mixture of behavior in the far infrared, making the total infrared luminosity estimation for a typical case ambiguous.

6. CONCLUSIONS

We have modeled the far infrared spectral energy distribution (SED) expected from Population II galaxies undergoing the first phase of vigorous star formation after the Population III stage. For the first 300 – 400 Myr, the interstellar dust in such systems will be silicate-rich, differing significantly from the dust in more mature galaxies. We have then compared the models with observations of galaxies as a function of redshift. We find:

- The modeled SEDs are shifted substantially to the bluer (“warmer”) wavelengths compared to the SEDs of local galaxies.
- Although other factors contribute, e.g., the high energy density in the galaxy, this behavior arises in part because of the relatively high emission efficiency of silicates between 8 and $60\mu\text{m}$.
- The SED of Haro 11 is similar to the theoretical prediction for silicate-rich dust with a small addition of carbon dust. Haro 11 is a local galaxy with a very young and vigorous starburst that probably reproduces the relevant conditions in the Population II galaxies.
- There is a progression with redshift in observed galaxy SEDs, from those resembling local ones at

$2 \leq z < 4$ to a closer resemblance to that of Haro 11 for $5 \leq z < 7$.

- Estimates of total infrared luminosities at $z \gtrsim 5$ based on measurements at 250, 350, and $500\mu\text{m}$ (i.e., with *Herschel* SPIRE) with templates that do not reflect the breadth of the Haro 11 SED may differ from those using it by 20 – 30 %.
- Estimates of the total infrared luminosities at $z \gtrsim 5$ (and hence star formation rates) with measurements near 1 mm in wavelength can vary by factors of 2 – 3 or more depending on the SED template used. Currently popular modified blackbodies or local templates can result in significant underestimates compared with those using Haro 11 as the template.

Further understanding of the far infrared SEDs at high redshift can come with measurements of hydrogen recombination lines to determine the populations of luminous stars independently of the far infrared and testing for consistency. These measurements will be enabled by *JWST*, which can measure both the Balmer and Paschen series lines. Use of secondary indicators of star formation, such as the radio-infrared relation, is problematic because their calibration may evolve with redshift. Direct measurements of the far infrared SEDs over the relevant wavelength region to probe Haro-11-like SEDs ($100 - 300\mu\text{m}$) will be challenging; the Space Infrared Telescope for Cosmology and Astrophysics (SPICA) will be helpful but in the end its contributions will be limited by confusion noise. The larger aperture of the Origins Space Telescope (OST) would allow extension of the understanding of these SEDs to significantly lower luminosities than is possible in other ways. More fully exploring the FIR frontier at the highest redshifts will crucially depend on the future availability of these next-generation facilities.

ACKNOWLEDGEMENTS

We thank Rob Kennicutt, Dan Marrone, Karl Missett, and Corentin Schreiber for helpful discussions. MEDR acknowledges support from PICT-2015-3125 of ANPCyT. VB acknowledges support from NSF grant AST-1413501. The work of GHR, IS, and JL was partially supported by NASA Grant NNX13AD82G, and that of IS was also partially supported by a Hubble Fellowship. We thank Alexander Ji for providing tabulated dust opacities for the dust model used here. This work makes use of the Yggdrasil code (Zackrisson et al. 2011), which adopts Starburst99 SSP models, based on Padova-AGB tracks (Leitherer et al. 1999; Vázquez & Leitherer 2005) for Population II stars.

REFERENCES

- Adamo, A., Ostlin, G., Zackrisson, E., et al. 2010, *MNRAS*, 407, 870
- Arendt, R. G., Dwek, E., Kober, G., Rho, J., & Hwang, U. 2014, *ApJ*, 786, 55
- Asano, R. S., Takeuchi, T. T., Hirashita, H. & Inoue, A. K. 2011, *ASP Conf. Ser.* "Why Galaxies Care about AGB Stars II, ed. Kerschbaum, Lebzelter, & Wing", 445, 523
- Asboth, V., Conley, A., Sayers, J., et al. 2016, *MNRAS*, 462, 1989
- Asmus, D., Hoenig, S. F., and Gandhi, P. 2016, *ApJ*, 822, 109
- B ethermin, M., Daddi, E., Magdis, G., et al. 2015, *A&A*, 573, A113
- Berta, S., Lutz, D., Santini, P., et al. 2013, * *, 551, A100
- Bradac, M., Garcia-Appadoo, D., Huang, K.-H., et al. 2017, *ApJ*, 836, 2
- Bressan A., Marigo P., Girardi L., et al. 2012, *MNRAS*, 427, 127
- Bromm, V., & Yoshida, N. 2011, *ARA&A*, 49, 373
- Bowler, R. A. A., Bourne, N., Dunlop, J. S., McLure, R. J., & McLeod, D. J. 2018, arXiv 1802.05720v1
- Casey, C. M., Berta, S., Bethermin, M., et al. 2012a, *ApJ*, 761, 139
- Casey, C. M. 2012b, *MNRAS*, 425, 3094
- Chakrabarti, S., & McKee, C. F. 2005, *ApJ*, 631, 792
- Chary, R., & Elbaz, D. 2001, *ApJ*, 556, 562
- Cherchneff, I., & Dwek, E. 2010, *ApJ*, 713, 1
- Chu, J. K., Sanders, D. B., Larson, K., et al. 2017, *ApJS*, 229, 25
- Ciesla, L., Boquien, M., Boselli, A., et al. 2014, *A&A*, 565, A128
- Combes, F., Rex, M., & Rowle, T. D. 2012, *A&A*, 538L, 4
- Cormier, D., Madden, S. C., Lebouteiller, V., et al. 2014, *A&A*, 564A, 121
- Cos, P., Krips, M., Neri, R., et al. 2011, *ApJ*, 740, 63
- da Cunha, E., Charmandaris, V., D az-Santos, T., Armus, L., Marshall, J. A., & Elbaz, D. 2010, *A&A*, 523, A78
- da Cunha, E., Groves, B., Walter, F., et al. 2013, *ApJ*, 766, 13
- Dale, D. A., & Helou, G. 2002, *ApJ*, 576, 159
- Dell'Agli, G., Garc a-Hern andez, D. A., Rossi, C., et al. 2014, *MNRAS*, 441, 1115
- Decarli, R., Walter, F., Venemans, B. P., et al. 2017, *Nature*, 545, 457
- Decarli, R., Walter, F., Venemans, B. P., et al. 2018, *ApJ*, 854, 97
- De Rossi, M. E., & Bromm, V. 2017, *MNRAS*, 465, 3668 (DB17)
- Di Criscienzo, M., Dell'Agli, F., Ventura, P., et al. 2014, *Mem. S. A. It.* 85, 578
- Dunlop, J. S., McLure, R. J., Biggs, A. D., et al., 2017, *MNRAS*, 466, 861
- Dwek, E., Staguhn, J., Arendt, R. G. Kovacks, A., Su, Ting, & Benford, D. J. 2014, *ApJL*, 788, 30
- Elbaz, D., Dickinson, M., Hwang, H. S., et al. 2011, *A&A*, 533, A119
- Elvis, M., Wilkes, B. J., McDowell, J. C., et al. 1994, *ApJS*, 95, 1
- Faisst, A. L., Capak, P. L., Yan, L., et al. 2017, *ApJ*, 847, 21
- Fan, X. 2009, *ASP Conf. Ser.*, 408, 439
- Frebel, A., & Bromm, V. 2012, *ApJ*, 759, 115
- Fudamoto, Y., Oesch, P. A., Schinnerer, E., et al. 2017a, *MNRAS*, 472, 483
- Fudamoto, Y., Ivison, R. J., Oteo, I. et al. 2017, *MNRAS*, 472, 2028
- Guseva N. G., Izotov, Y. I., Fricke, K. J. & Henkel, C. 2012, *A&A*, 541, 115
- Hashimoto T., Garel, T., Guiderdoni, B., et al. 2017, *A&A*, 608, 10
- Hayward, C. C., Keres, D., Jonsson, P., et al. 2011, *ApJ*, 743, 159
- Huang, J.-S., Rigopoulou, D., Magdis, G., et al. 2014, *ApJ*, 784, 52
- Hutchings, J. B. 2003, *AJ*, 125, 1053
- Hutchings, J. B. 2005, *PASP*, 117, 1250
- Jaacks, J., Finkelstein, S. L., & Bromm, V. 2018, *MNRAS*, 475, 3883
- James, B. L., Tsamis, Y. G., Walsh, J. R., Barlow, M. J., & Westmoquette, M. S. 2013, *MNRAS*, 430, 2097
- Ji, A. P., Frebel, A., & Bromm, V. 2014, *ApJ*, 782, 95
- Ji, A. P., Frebel, A., & Bromm, V. 2015, *MNRAS*, 454, 659
- Kirkpatrick, A., Pope, A., Sajina, A., et al. 2015, *ApJ*, 814, 9
- Koike, C., Chihara, H., Tsuchiyama, A., Suto, H., Sogawa, H., & Okuda, H. 2003, *A&A*, 399, 1101
- Kriek, M., Conroy, C., van Dokkum, P. G., et al. 2016, *Nature*, 540, 248
- Lagache, G., Cousin, M., & Chatzikos, M. 2018, *A&A*, 609, A130
- Leipski, C., Meisenheimer, K., Walter, F., et al. 2014, *ApJ*, 785, 154
- Leitherer, C., et al. 1999, *ApJS*, 123, 3
- Lyu, J., Rieke, G. H., & Alberts, S. 2016, *ApJ*, 816, 85
- Lyu, J., & Rieke, G. 2017a, *ApJ*, 835, 257
- Lyu, J., & Rieke, G. 2017b, *ApJ*, 841, 76
- Lyu, J., & Rieke, G. 2018, *ApJ*, 866, 92
- Ma, J., Gonzalez, A. H., Vieira, J. D., et al. 2015, *ApJ*, 812, 88
- Ma, J., Gonzalez, A. H., Vieira, J. D., et al. 2016, *ApJ*, 832, 114
- Magdis, G. E., Daddi, E., B ethermin, M., et al. 2012, *ApJ*, 760, 6
- Magnelli, B., Lutz, D., Santini, P., et al. (2012, *A&A*, 539A, 155
- Mainali, R., Kollmeier, J., Stark, D., et al. 2017, *ApJ*, 836, L14
- Marassi, S., Schneider, R., Limongi, M., et al. 2015, *MNRAS*, 454, 4250
- Matthee, J., Sobral, D., Boone, F., et al. 2017, *ApJ*, 851, 145
- McLeod, K. K., & Bechtold, J. 2009, *ApJ*, 704, 415
- Mechtley, M., Windhorst, R. A., Ryan, R. E., et al. 2012, *ApJL*, 756, 38
- Michalowski, M. J., Murphy, E. J., Hjorth, J., et al. 2011, *ASP Conf Series*, 446, 387
- Michalowski, M. J. 2015, *A&A*, 577A, 80
- Negrello, M., Hopwood, R., De Zotti, G., et al. 2010, *Science*, 330, 800
- Nozawa, T., Kozasa, T. 2013, *ApJ*, 776, 24
- Ostlin, G., Marquart, T., Cumming, R. J., et al. 2015, *A&A*, 583A, 55
- Oteo, I., Ivison, R. J., Negrello, M., et al. 2017, arXiv 1709.0419v1
- Oteo, I., Ivison, R. J., Dunne, L., et al. 2018, *ApJ*, 856, 72
- Pentericci, L., Carniani, S., Castellano, M., et al. 2016, *ApJ*, 829, 11
- Popescu, C. C., Tuffs, R. J., Dopita, M. A., Fischera, J., Kylafis, N. D., & Madore, B. F. 2011, *A&A*, 527, A109
- R emy-Ruyer, A., Madden, S. C., Galliano, F., et al. 2013, *A&A*, 557, A95
- R emy-Ruyer, A., Madden, S. C., Galliano, F., et al. 2015, *A&A*, 582, A121
- Riechers, D. A., Carilli, C. L., Capak, P. L., et al. 2014, *ApJ*, 796, 84
- Riechers, D. A., Leung, T. K. D., Ivison, R. J., et al. 2017, *ApJ*, 850, 1
- Rieke, G. H., Alonso-Herrero, A., Weiner, B. J., et al. 2009, *ApJ*, 692, 556
- Roseboom, I. G., Ivison, R. J., Grene, T. R., et al. 2012, *MNRAS*, 419, 2758
- Rujopakarn, W., Rieke, G. H. Eisenstein, D. J., & Juneau, S. 2011, *ApJ*, 726, 93
- Rujopakarn, W., Rieke, G. H. Weiner, B. J., et al. 2013, *ApJ*, 767, 73
- Saintonge, A., Lutz, D., Genzel, R., et al., 2013, *ApJ*, 778, 2
- Sauvage, M., & Thuan, T. X. 1992, *ApJ*, 396, L69
- Schneider, R., Hunt, L., & Valiante, R. 2016, *MNRAS*, 457, 1842
- Schreiber, C., Elbaz, D., Pannella, M., Ciesla, L., Wang, T., & Franco, M. 2018, *A&A*, 609A, 30
- Shiple, H. V., Papovich, C., Rieke, G. H., Brown, M. J. I., & Moustakas, J. 2016, *ApJ*, 818, 60
- Shu, X. W., Elbaz, D. Bourne, N., et al. 2016, *ApJS*, 222, 4
- Sklias, P., Zamojski, M., Schaerer, D., et al. 2014, *A&A*, 561A, 149
- Smit, R., Bouwens, R. J., Carniani, S., et al. 2018, *Nature*, 553, 178
- Smolcic, V., Karim, A., Miettinen, O., et al. 2015, *A&A*, 576A, 127
- Spilker, J. S., Marrone, D. P., Aravena, M., et al. 2016, *ApJ*, 826, 112
- Stalevski, M., Ricci, C., Ueda, Y., et al. 2016, *MNRAS*, 458, 2288
- Stark, D., Ellis, R., Charlot, S., et al. 2017, *ApJ*, 464, 469
- Strandet, M. L., Weiss, A., Vieira, J. D., et al. 2016, *ApJ*, 822, 80
- Symeonidis, M., Page, M. J., Seymour, N., et al. 2009, *MNRAS*, 397, 1728
- Symeonidis, M., Vaccari, M., Berta, S., et al. 2013, *MNRAS*, 431, 2317

- Targett, T. A., Dunlop, J. S., & McLure, R. J. 2012, *MNRAS*, 420, 3621
- Vázquez, G. A., & Leitherer, C. 2005, *ApJ*, 621, 695
- Ventura, P., di Criscienzo, M., Schneider, R., et al. 2012a, *MNRAS*, 420, 1442
- Ventura, P., di Criscienzo, M., Schneider, R., et al. 2012b, *MNRAS*, 424, 2345
- Ventura, P., Dell’Agli, F., Schneider, R., et al. 2014, *MNRAS*, 439, 977
- Ventura, P., Stanghellini, L., Dell’Agli, F., Garcia-Hernandez, D. A., & Di Criscienzo, M. 2015, *MNRAS*, 452, 3679
- Wang, Ran, Carilli, C. L., Beelen, A., et al. 2007, *AJ*, 134, 617
- Wang, Ran, Wagg, J., Carilli, C. L., et al. 2008, *AJ*, 135, 1201
- Wang, R., Wagg, J., Carilli, C. L., et al. 2013, *ApJ*, 773, 44
- Wang, T., Elbaz, D., Schreiber, C., et al. 2016, *ApJ*, 816, 84
- Weiss, A., De Breuck, C., Marrone, D. P., et al. 2013, *ApJ*, 767, 88
- Willott, C. J., Omont, A., & Bergeron, J. 2013, *ApJ*, 770, 13
- Willott, C. J., Bergeron, J. & Omont, A. 2017, *ApJ*, 850, 108
- Wu, Y., Charmandaris, V., Hao, L., et al. 2006, *ApJ*, 639, 157
- Xu, L., Rieke, G. H., Egami, E., et al. 2015, *ApJS*, 219, 18
- Yuan, F., Buat, V., Burgarella, D., et al. 2015, *A&A*, 582A, 90
- Zackrisson, E., Rydberg, C. E., Schaerer, D., Östlin, G., & Tuli M. 2011, *ApJ*, 740, 13
- Zavala, J. A., Montana, A., Hughes, D. H., et al. 2018, *NatureAst*, 2, 56
- Zubko, V. G., Mennella, V., Colangeli, L., & Bussoletti, E. 1996, *MNRAS*, 282, 1321

TABLE 1
GALAXIES WITH FIR SED MEASUREMENTS

name	z	reference
GH500.13	1.99	Shu et al. (2016)
GH500.28	1.99	Shu et al. (2016)
GH500.12	2.00	Shu et al. (2016)
HUDF composite	~ 2	Dunlop et al. (2017)
GH500.16	2.02	Shu et al. (2016)
1HERMES X24 J095917.28+021300.4	2.101	Casey et al. (2012a)
GH500.21	2.13	Shu et al. (2016)
COSMOS	2.25	Béthermin et al. (2015)
SPT0002-52	2.3523	Strandet et al. (2016)
GH500.33	2.41	Shu et al. (2016)
GH500.14a	2.47	Shu et al. (2016)
GH500.26	2.49	Shu et al. (2016)
Red HIEROS	~ 2.5	Wang et al. (2016)
GH500.9	2.57	Shu et al. (2016)
1HERMES X24 J095948.00+024140.7	2.60	Casey et al. (2012a)
GH500.20	2.67	Shu et al. (2016)
COSMOS	2.75	Béthermin et al. (2015)
SPT2349-50	2.877	Strandet et al. (2016)
CANDELS stack	3	Schreiber et al. (2018)
SDP81	3.04	Negrello et al. (2010), Yuan et al. (2015)
SPT2357-51	3.0703	Strandet et al. (2016)
Eye	3.074	Saintonge et al. (2013), Yuan et al. (2015)
SPT0103-45	3.0917	Weiss et al. (2013), Yuan et al. (2015)
SPT2307-50	3.108	Strandet et al. (2016)
1HERMES X24 J033136.96275510.9	3.145	Casey et al. (2012a)
SMMJ16354+66114	3.188	Magnelli et al. (2012), Yuan et al. (2015)
A68/nn4	3.19	Sklias et al. (2014), Yuan et al. (2015)
COSMOS	3.25	Béthermin et al. (2015)
1HERMES X24 J160603.63+541245.1	3.331	Casey et al. (2012a)
SPT0529-54	3.3689	Weiss et al. (2013), Yuan et al. (2015)
1HERMES X1.4 J123536.28+623019.9	3.38	Casey et al. (2012a)
SPT0532-50	3.3988	Weiss et al. (2013), Yuan et al. (2015)
1HERMES X24 J160802.63+542638.1	3.415	Casey et al. (2012a)
1HERMES X24 J160539.72+534450.3	3.546	Casey et al. (2012a)
1HERMES X1.4 J100024.00+021210.9	3.553	Casey et al. (2012a)
1HERMES X1.4 J123622.58+620340.3	3.579	Casey et al. (2012a)
SPT2147-50	3.7602	Weiss et al. (2013), Yuan et al. (2015)
HELMS-RED-31	3.798	Asboth et al. (2016), Oteo et al. (2017)
1HERMES X24 J160639.40+533558.4	3.801	Casey et al. (2012a)
NGHP-246114	3.847	Fudamoto et al. (2017b)
SPT2340-59	3.864	Strandet et al. (2016)
1HERMES X1.4 J100111.52+022841.3	3.975	Casey et al. (2012a), Yuan et al. (2015)
SGP-354388	4.002	Fudamoto et al. (2017b), Oteo et al. (2018)
GH500.18	4.04	Shu et al. (2016)
GN500.27a	4.04	Shu et al. (2016)
GN10	4.05	Huang et al. (2014)
GN20	4.05	Huang et al. (2014)
GN20.2	4.05	Huang et al. (2014)
G1	4.05	Roseboom et al. (2012), Yuan et al. (2015)
SPT0418-47	4.2248	Weiss et al. (2013), Yuan et al. (2015)
SPT0113-46	4.2328	Weiss et al. (2013), Yuan et al. (2015)
HATLASID141	4.24	Cox et al. (2011), Yuan et al. (2015)
SGP-261206	4.242	Fudamoto et al. (2017b), Oteo et al. (2017)
SPT2311-54	4.2795	Strandet et al. (2016)
SPT0345-47	4.2958	Weiss et al. (2013), Yuan et al. (2015)
SPT2349-56	4.304	Strandet et al. (2016)
Blue HIEROS	~ 4.4	Wang et al. (2016)
NGP-190387	4.42	Fudamoto et al. (2017b)
SGP-196076	4.425	Fudamoto et al. (2017b)
SPT2103-60	4.4357	Weiss et al. (2013), Yuan et al. (2015)
X24 J095916.08+021215.3	4.454	Casey et al. (2012a), Yuan et al. (2015)
SPT0441-46	4.4771	Weiss et al. (2013), Yuan et al. (2015)
1HERMES X1.4 J104722.56+590111.7	4.521	Casey et al. (2012a), Yuan et al. (2015)
G09-81106	4.53	Fudamoto et al. (2017b)
SPT2146-55	4.5672	Weiss et al. (2013), Yuan et al. (2015)
Vd-17871	4.622	Smolcic et al. (2015), Yuan et al. (2015)
AzTEC1	4.64	Huang et al. (2014)
1HERMES X1.4 J104649.92+590039.6	4.71	Casey et al. (2012a)
SPT2335-53	4.757	Strandet et al. (2016)
SPT2132-58	4.7677	Weiss et al. (2013), Yuan et al. (2015)
NGP-284357	4.894	Fudamoto et al. (2017b)
1HERMES X24 J161506.65+543846.9	4.952	Casey et al. (2012a)
J0338+0021	5.00	Lyu et al. (2016)
J1204-0021	5.03	Lyu et al. (2016)

TABLE 1 — *Continued*

name	z	reference
J0756+4104	5.09	Lyu et al. (2016)
HeLMS-RED-4	5.162	Asboth et al. (2016)
HLSA773	5.24	Combes et al. (2012), Yuan et al. (2015)
SPT2319-55	5.2929	Strandet et al. (2016)
AzTEC3	5.30	Huang et al. (2014)
J1202+3235	5.31	Lyu et al. (2016)
J1340+2813	5.34	Lyu et al. (2016)
ADFS-27	5.655	Riechers et al. (2017)
SPT0346-52	5.6559	Weiss et al. (2013), Yuan et al. (2015), Ma et al. (2015, 2016)
SPT0243-49	5.699	Weiss et al. (2013), Yuan et al. (2015)
SPT2353-50	5.576	Strandet et al. (2016)
J0927+2001	5.77	Lyu et al. (2016)
SPT0459-59	5.7993	Weiss et al. (2013), Yuan et al. (2015)
SPT2351-57	5.811	Strandet et al. (2016)
G09-83808	6.027	Fudamoto et al. (2017b), Zavala et al. (2018)
HFLS3	6.34	Riechers et al. (2014), Yuan et al. (2015)

TABLE 2
SPECTRAL ENERGY DISTRIBUTION OF HARO 11

wavelength (μm)	Jy
3.00262	2.04E-02
3.00954	2.04E-02
3.01648	2.05E-02
3.02343	2.06E-02
3.03040	2.06E-02
3.03739	2.07E-02
3.04439	2.07E-02
3.05141	2.08E-02

A. SPECTRAL ENERGY DISTRIBUTION OF HARO 11

We provide a digital form of the infrared spectral energy distribution of Haro 11 in Table 2. The first few entries are shown here for illustrative purposes.

B. POTENTIAL AGN CONTRIBUTIONS TO THE FIR SED

In this appendix, we address whether the points between 10 and 50 μm derived by fitting high redshift quasar observations could give an overestimated measure of the galaxy output in this spectral range. Lyu et al. (2016) tested fitting the far infrared SEDs of high redshift quasars with a combination of a FIR-star-formation-removed Elvis et al. (1994)-like quasar continuum template and Rieke et al. (2009) star forming templates for $\log(L(\text{TIR})) = 11.25$ and 12.50 and found that both types of fit fell far short of the measurements in the 10 – 50 μm range. In contrast, the Haro 11 SED gave a good fit. If the “local” templates are used to fit the measurements of these quasars, then the quasar must be far brighter than the Elvis et al. SED in this spectral range to account for the output in the mid-infrared.

All of the high-redshift quasars are of very luminous type-1 AGNs without evidence of significant reddening (the strong UV continuum of this type is essential to their discovery). Lyu & Rieke (2017a,b) evaluated the AGN infrared SEDs of such quasars. In the first reference they found two general cases where the mid-infrared continua can have significantly less output in the 10 – 20 μm range than the Elvis template and they showed that this behavior was independent of redshift up through $z \sim 6$. They dubbed these cases “warm dust deficient (WDD)”, meaning a typical Elvis-like peak near 3 μm but a SED that drops more rapidly than the Elvis one toward longer wavelengths; and “hot dust deficient (HDD)”, which does not have the 3 μm feature but simply drops relative to the Elvis template from there to longer wavelengths. If we have used the Elvis template where one of these alternatives would be appropriate, then we will have underestimated the potential star-forming contribution in the 10 – 50 μm range.

B.1. Association of the Warm Dust with Star Formation

Nonetheless, it is worth considering in more detail the possibility that the warm far infrared spectral component that produces the deviation from “local” templates in the 10 – 50 μm range might be dust heated by the quasar. Lyu & Rieke (2017b) advanced a number of arguments that show that the intrinsic SEDs of Type 1 quasars drop at wavelengths longer than 20 – 30 μm . Some local AGNs have an additional emission component due to polar dust that boosts the emission in this region (e.g., Asmus et al. 2016, Lyu & Rieke 2018), but this component is largely missing in more luminous AGN, probably because of the larger radiation pressure in their polar directions that tends to eject material rapidly. Hypothesizing that this warm component is present in all six of the high redshift quasars used to derive the stellar-powered SED in this paper requires that their SEDs differ significantly from those of lower-redshift quasars, which would be contrary to all the evidence that the SEDs are identical, including in the infrared (e.g., Fan 2009; Lyu & Rieke 2017a).

Figure 11 illustrates the issue specifically for these six quasars. It shows that the strongest excesses above the quasar continuum template in the 10 – 50 μm range are associated with powerful excesses at the longer far infrared wavelengths. These latter excesses almost certainly arise from dust heated by star formation in the host galaxies. This relationship is not expected if the quasar itself is responsible for the 10 – 50 μm emission, in which case it would be expected to be independent of the output of the host galaxies.

B.2. Energy Balance and the Warm Dust

The hypothesis that this emission arises from heating by the quasar can also be tested for these specific objects by energy balance: is the expected optical to UV luminosity of the quasar sufficiently larger than the infrared luminosity to make it plausible that the infrared arises through heating of dust by the quasar? In general, the value of the ratio of these quantities should reveal the covering fraction of dusty structures around the AGN central engine. We have applied this test to the six quasars in this study. We used the $\log(L(\text{TIR})) = 12.25$ template to represent the star formation in the host galaxies, since it provides a rough fit at the long wavelengths. To it, we added the output of a single temperature grey-body with a wavelength-dependent emissivity proportional to $\lambda^{-\beta}$, with $\beta = 2$. This fit should produce a lower limit to the luminosity of the warm component since it produces a SED peaked relatively sharply at the critical wavelengths; addition of components over a range of temperatures would increase the derived luminosity, for example, since they would add emission at wavelengths not well constrained by the data. We computed the energy

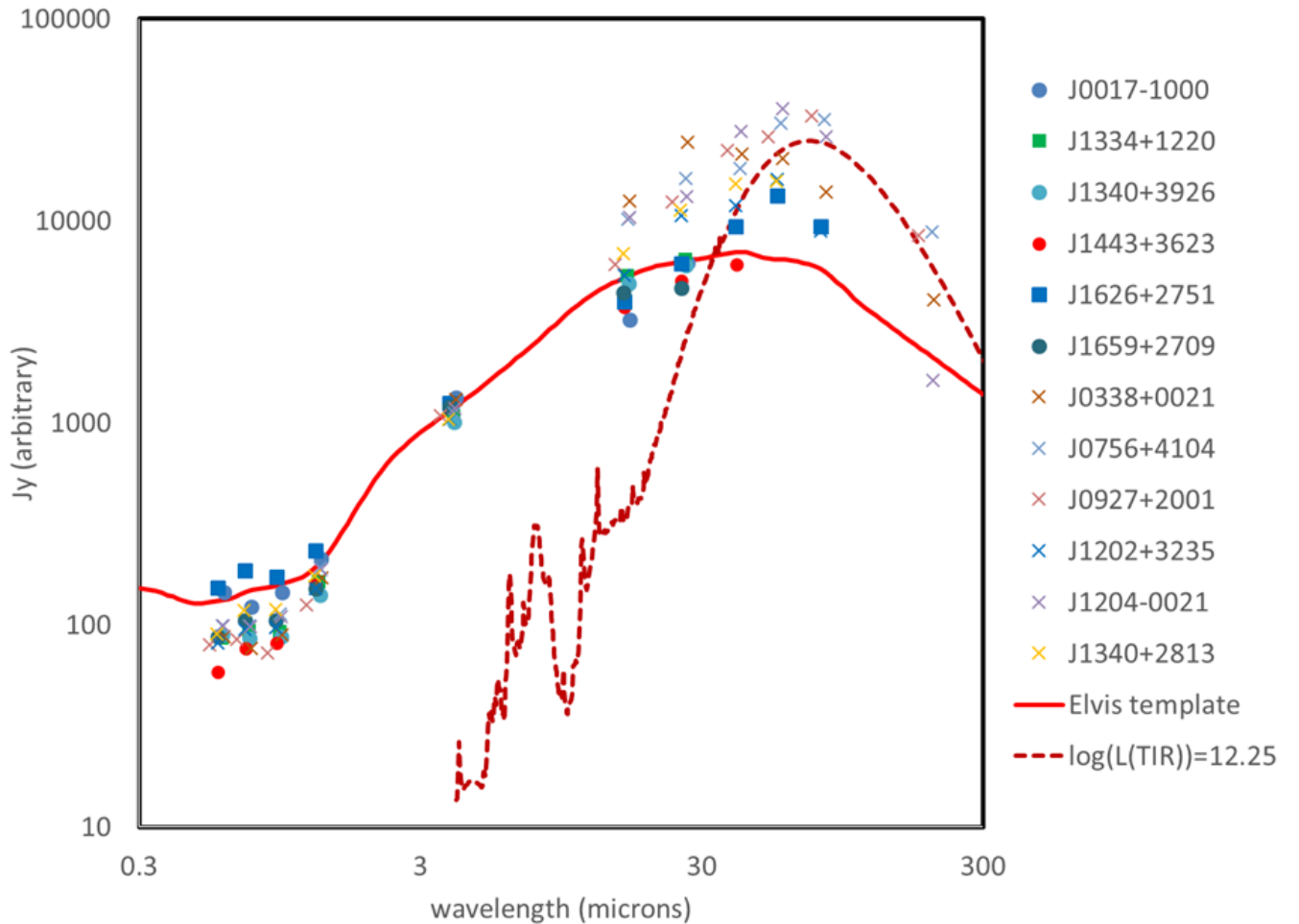


FIG. 11.— Photometry of all high- z quasars in Leipski et al. (2014) with usable signal to noise (> 3) in the far infrared. The measurements have been shifted to the rest frame and normalized near $4 \mu\text{m}$. An Elvis SED has been normalized to the measurements at this wavelength and a local star forming template with $\log(L(\text{TIR})) = 12.25$ is shown roughly fitted to the points near the peak of this template. The galaxies with the largest far infrared excesses above the quasar continuum, lying around the peak of this local template (x symbols), are also the ones with significant excesses above the Elvis SED in the $10 - 50 \mu\text{m}$ range.

balance assuming that all the luminosity at wavelengths short of $1.1 \mu\text{m}$ was available to heat the warm dust and that all the luminosity at longer wavelengths was from such heated dust except for the contribution from the ULIRG template. The rationale for this approach can be found in Lyu & Rieke (2017b). The results are in Table 3, shown as lower limits because of the potential underestimate of the warm component luminosity due to the assumption of a single temperature.

With the simple assumption of isotropic emission, the first three quasars listed are already in violation of the expectations from energy balance. A more rigorous comparison needs to take account of the expected anisotropies in the emission by the central engine of an AGN. This case has been modeled by Stalevski et al. (2016), who studied the relation between the covering fraction and the reradiated accretion disk emission with a torus that is optically thick in the mid-IR. Their simulations indicate how the luminosity changes with different parameter values for the torus. For the cases where the predicted SED matches that observed, the upper limit to the ratio of reradiated to central engine luminosity is ~ 0.75 (see the further discussion in Lyu & Rieke 2017b). All six quasars are above this upper limit (see Table 2).

The quasars in Table 3 constitute about half of those in Leipski et al. (2014) with useful far infrared measurements, i.e. detections at 3:1 or more signal to noise in multiple bands. It is unlikely from an energy balance perspective that half of the quasars with useful Herschel data both have some unique circum-nuclear structure to emit in the mid-IR and are also pushing the limits of energy balance. Of course the energy balance argument could be circumvented if the ultraviolet spectra of these quasars are anomalously bright, but then we need to invoke two departures from typical quasar behavior (UV and mid-IR), when all the evidence to date is that the high-redshift quasars are identical in all observables to their lower redshift counterparts (e.g., Fan 2009).

TABLE 3
ENERGY BALANCE BETWEEN UV HEATING AND POSSIBLE WARM DUST COMPONENT

quasar	warm dust temperature	IR reradiated luminosity/ UV heating luminosity
J0338+0021	100	> 1.15
J0756+4104	120	> 1.23
J0927+2001	120	> 1.32
J1202-3235	125	> 0.88
J1204-0021	80	> 0.86
J1340+2813	110	> 0.85